



Comparison of focused ion beam versus nano-scale X-ray computed tomography for resolving 3-D microstructures of porous fuel cell materials



E.A. Wargo^a, T. Kotaka^b, Y. Tabuchi^b, E.C. Kumbur^{a,*}

^aElectrochemical Energy Systems Laboratory, Department of Mechanical Engineering and Mechanics, Drexel University, Philadelphia, PA 19104, USA

^bNissan Research Center, Nissan Motor Co., Ltd., Yokosuka, Kanagawa 237-8523, Japan

HIGHLIGHTS

- Unique features and limitations of FIB-SEM and nano-CT techniques are compared.
- A sample of MPL used in PEFC is selected for characterization and comparison.
- Acquired images, segmentation and resulting 3D reconstructions are analyzed.
- Structure-related properties calculated from these 3D datasets are compared.
- Several items for consideration are highlighted to promote best practices.

ARTICLE INFO

Article history:

Received 26 February 2013

Received in revised form

27 April 2013

Accepted 29 April 2013

Available online 13 May 2013

Keywords:

Focused ion beam

X-ray

Computed tomography

Nanotomography

Microstructure

Polymer electrolyte fuel cell

ABSTRACT

Focused ion beam-scanning electron microscopy (FIB-SEM) and nano-scale X-ray computed tomography (nano-CT) have emerged as two popular nanotomography techniques for quantifying the 3-D microstructure of porous materials. The objective of this study is to assess the unique features and limitations of FIB-SEM and nano-CT in capturing the 3-D microstructure and structure-related transport properties of porous fuel cell materials. As a test case, a sample of a micro-porous layer used in polymer electrolyte fuel cells is analyzed to obtain 3-D microstructure datasets using these two nanotomography techniques. For quantitative comparison purposes, several key transport properties are determined for these two datasets, including the porosity, pore connectivity, tortuosity, structural diffusivity coefficient, and chord length (i.e., void size) distributions. The results obtained for both datasets are evaluated against each other and experimental data when available. Additionally, these two techniques are compared qualitatively in terms of the acquired images, image segmentation, and general systems operation. The particular advantages and disadvantages of both techniques are highlighted, along with suggestions for best practice.

© 2013 Elsevier B.V. All rights reserved.

1. Introduction

Polymer electrolyte fuel cells (PEFCs) are a promising technology for use as an alternative power source in a wide range of applications. To improve the performance and durability of PEFCs, many research efforts are focused on understanding the complex internal structure (henceforth referred to as “microstructure”) and related transport behavior of porous PEFC components such as the diffusion media (DM), micro-porous layer (MPL) and catalyst layer (CL). Recognizing the minute length scales and heterogeneous nature of these components, several microstructure quantification

techniques have emerged to capture the internal structure of these materials.

Two popular techniques which offer 3-D quantification of PEFC materials at nano-scale resolution are focused ion beam-scanning electron microscopy (FIB-SEM) and nano-scale X-ray computed tomography (nano-CT). Both FIB-SEM and nano-CT have been shown to be particularly useful for capturing the fine structures of porous PEFC components such as the MPL [1–4] and CL [5–7], as well as materials used in other fuel cell types and fields (e.g., solid oxide fuel cells (SOFCs)) [8–14]. In terms of operation, FIB-SEM combines the imaging capabilities of SEM with the precise milling and cross-sectioning ability of a FIB, enabling serial-sectioning of a sample of interest to produce high-resolution 3-D reconstructions [1–6,8–13,15]. On the other hand, nano-CT systems

* Corresponding author. Tel.: +1 215 895 5871; fax: +1 215 895 1478.

E-mail address: eck32@drexel.edu (E.C. Kumbur).

operate based on the principles of a conventional X-ray CT system with the addition of finer focusing components and a zone plate objective, which allows for capturing the 3-D microstructure of a material at nano-scale resolutions by non-destructive means [7,11,14].

In fuel cell studies, the measured 3-D structure of a material is often desired for pore-scale modeling [1,13] and materials characterization efforts [1–14,16] to determine the characteristic relationship between the internal morphology and related mass/charge transport behavior of a particular fuel cell component. While microstructure quantification combined with pore-scale modeling can be quite useful for evaluating the transport characteristics of a given material, the accuracy of the modeling domain (i.e., measured 3-D structure) plays a key role in dictating the quality of the results obtained from pore-scale analyses. Numerous factors can impact the quality of the measured 3-D structure, such as sample preparation, image acquisition, signal quality, data processing, segmentation, reconstruction, etc. Recently, a few studies have been conducted to investigate one or more of these factors which affect the quality of the data measured by these techniques. For instance, Gunda et al. [10] explored the effects of various image processing procedures (e.g., grayscale threshold value, median filter radius, and smoothing filter) on the calculation of porosity, internal surface area, and effective electronic conductivity/gas diffusivity for an SOFC electrode characterized using FIB-SEM. Another example of such a study was conducted by Shearing et al. [11], in which an SOFC electrode was characterized using both FIB-SEM and nano-CT, and the measured microstructures were compared in terms of porosity and qualitative features. Although these studies provide useful insight, more understanding with regard to their limitations is needed to better evaluate the effectiveness of these two techniques in capturing the myriad microstructural features of fuel cell materials.

Motivated by this need, the objective of this study is to assess the unique features and limitations of FIB-SEM and nano-CT in capturing the 3-D microstructure and structure-related transport properties of porous fuel cell materials. An MPL specimen with nano-scale pore features was selected as a test sample, and its microstructural features were analyzed using these two nanotomography techniques. The datasets were compared in terms of their geometric properties, transport behavior, and overall microstructural features. Several key structure-related properties were determined for comparison, including porosity, pore connectivity, and distributions of tortuosity, structural diffusivity coefficient, and chord length (i.e., pore size). Additionally, these two techniques were compared based on the acquired images and system operation, and the respective advantages and disadvantages are highlighted.

1.1. FIB-SEM vs. nano-CT: general comparison

Although FIB-SEM and nano-CT both yield a stack of 2-D images composed of pixels with varying grayscale intensity, they are quite different in terms of system operation and capabilities. Table 1 summarizes the main differences and important considerations for each technique in general, including some values specific to this study. One of the key differences between these two techniques is that FIB-SEM is a destructive technique, in which slices of the material are physically milled away by the FIB to reveal successive cross sections which are imaged with the SEM. On the contrary, nano-CT is arguably a non-destructive technique; however, recent studies have shown that the synchrotron radiation used commonly in X-ray CT systems can affect some of the properties of PEFC components such as surface wettability, mechanical strength, etc. [17], although the effect on the overall solid morphology of the material is minimal.

Table 1
Comparison of the FIB-SEM and nano-CT techniques.

	FIB-SEM	Nano-CT
Time	~5–8 h for sample preparation and dataset acquisition in this study	~35 h in this study
Resolution	20 nm/pixel (~10 nm/pixel state-of-the-art)	~50 nm spatially, 32 nm/pixel (roughly state-of-the-art)
Field of View	~15 μm (x and y) at 20 \times magnification, but limited in slicing direction (z)	~15 μm (x, y, and z) at 50 nm spatial resolution
General Considerations	<ul style="list-style-type: none"> • Destructive • Excessive brightness from edge effect • Requires impregnation of sample pores for best results • Requires vacuum 	<ul style="list-style-type: none"> • Non-destructive • Low contrast • Does not require impregnation of sample pores • Vacuum not required

At present, neither FIB-SEM nor nano-CT is capable of distinguishing the carbon particles from PTFE or ionomer in PEFC materials (such as the MPL or CL) due to the limited resolution and/or phase contrast issues. While technological advancements may alleviate this limitation in the near future, it is possible that the resolutions of FIB-SEM and nano-CT may never reach levels which are high enough to clearly visualize the individual carbon particles (~30 nm average diameter) and PTFE nano-films within the material. For example, the maximum resolutions of state-of-the-art FIB-SEM and nano-CT systems are approximately 10 and 32 nm/voxel, respectively. In the case of FIB-SEM, the slice thickness/resolution is dependent on the FIB effective source size, which is generally on the order of 5 nm in diameter [15]. While higher resolutions are obtainable via SEM and can be interpolated between slices, the slice thickness (typically no less than 10 nm) ultimately limits the overall resolution of the system. Even though the resolutions of FIB-SEM and nano-CT may be near or higher than the feature sizes of the constituent material phases, they may still not be high enough to accurately resolve the phase distributions within the microstructure. For instance, Rüger et al. [12] observed that a resolution of 20–30 voxels per particle diameter was necessary to obtain reliable surface area estimates for a test microstructure. While such a high level of resolution may not be necessary for many 3-D imaging studies, even a more reasonable resolution of 5–10 voxels per feature size is currently unattainable by FIB-SEM or nano-CT to thoroughly investigate PEFC materials.

Although different phases (e.g., PTFE, ionomer, carbon particles) in PEFC materials are difficult to quantify in 3-D, the constituent phases of other materials may be differentiable by using these two techniques. For example, in the case of Ni-yttria stabilized zirconia (Ni-YSZ) anodes used in SOFCs, the Ni and YSZ phases can be distinguished during FIB-SEM characterization by use of an energy selective back scatter detector [11] or an energy dispersive X-ray spectroscopy (EDX) correlation image [13]. Similarly, Shearing et al. [14] demonstrated identification of the Ni and YSZ phases of an SOFC anode using X-ray adsorption edge spectroscopy in conjunction with nano-CT. For PEFC materials, the main challenge associated with differentiation of the individual phases stems from the poor contrast between the material phases (e.g., carbon particles vs. PTFE) which have similarly low atomic numbers.

Since FIB-SEM reconstructions are generally composed of a stack of SEM images, the void/solid interface of porous materials typically suffers from excessive brightness due to the edge effect of SEM, in which electrons are more easily excited from the edge of a solid feature. This often complicates the segmentation of SEM images into the pore (void) and solid phases, but can be alleviated by

impregnating the pore network with an appropriate contrast material (e.g., epoxy) [13]. The impregnation of the pores can also help to prevent erroneous segmentation by ensuring that only the cross section of a pore in the slice (i.e., plane) of interest is imaged via SEM, rather than the internal topography of the pore beyond the slice of interest. Additionally, it may prevent any solid material beyond the plane of interest from falling prematurely during serial sectioning. However, one issue with pore impregnation is the determination of an appropriate impregnation material, which depends on the chemical composition, size of pores, and fragility of the tested material. Pore impregnation is also difficult if the connectivity of the pore network is particularly low. In the case of nano-CT, sufficient contrast can typically be achieved between solid and void, and pore impregnation would likely complicate the imaging process.

Another point to consider is the fact that FIB-SEM must be conducted under vacuum, while nano-CT does not require vacuum conditions. This feature, combined with the non-destructive nature of nano-CT, makes it a promising technique for imaging PEFC components under realistic fuel cell operating conditions, pending future improvements in the temporal resolution of nano-CT. Eller et al. [18] recently demonstrated imaging of liquid water in PEFCs during operation using X-ray CT with micron-scale resolution. Additionally, since it is a non-destructive technique, nano-CT can also be used for studying the evolution of microstructure as a function of the aging of a material due to sintering, thermal cycling, etc.

2. Method of approach

In this study, an MPL sample manufactured in-house was chosen for characterization by FIB-SEM and nano-CT. The tested MPL sample is composed of polytetrafluoroethylene (PTFE) and acetylene black carbon particles, with an overall thickness of ~ 100 microns and pore sizes primarily below 500 nm, which makes it a very good candidate for testing the limitations of FIB-SEM and nano-CT with regard to PEFC materials. In terms of the approach followed, the stacks of images obtained by FIB-SEM and nano-CT were first post-processed and segmented to separate the pore (void) and solid phases. 3-D reconstructions were then assembled from the segmented FIB-SEM and nano-CT data. Using in-house microstructure analysis algorithms, key structure-related properties were determined for both datasets and compared against each other. The method of approach followed for assessment of these two techniques is shown in Fig. 1, and each step is detailed below.

2.1. Dataset acquisition via FIB-SEM and nano-CT

The microstructure of the MPL sample was first quantified using an FEI Strata™ DB 235 FIB-SEM, in a manner similar to that described in our previous publications [2–4]. Prior to the serial sectioning and imaging of the sample, a 1.5 μm layer of platinum was deposited over the volume of interest to prevent beam damage. The volume of interest was then exposed as a peninsula to minimize shadowing effects during image acquisition. A total of 200 image slices were captured by serial sectioning (500 pA/30 kV) with a slice thickness of 20 nm and an SEM resolution of ~ 15 nm/pixel. The SEM was operated in ultrahigh-resolution mode at 10 kV using a through-the-lens detector to maximize image clarity. Four distinct datasets were obtained in this manner from separate locations on the sample, each capturing a volume of $\sim 7 \times 11 \times 3 \mu\text{m}^3$.

A 3-D microstructure of the MPL sample was also captured using a nano-CT system (UltraXRM-L200, Xradia Inc., Pleasanton, CA). The nano-CT equipment employed in this study uses an X-ray beam

(operated in this study at 40 kV/30 mA), energy filter, capillary condenser, Fresnel zone plate objective, Zernike phase ring, and detector [7]. The Zernike phase contrast imaging mode allowed for the enhancement of the MPL's constituent materials, which have generally low atomic numbers. In terms of sample preparation, a 15 μm cubic piece of the in-house MPL sample was cut by FIB milling and fixed at the tip of a tungsten wire by epoxy adhesive. This sample was then analyzed using the nano-CT system with a 15 μm field of view and a pixel resolution of 32 nm, resulting in a single captured volume of $\sim 5.8 \times 5.8 \times 5.8 \mu\text{m}^3$.

By tuning system magnification or resolution, comparable fields of view ($\sim 15 \mu\text{m}$) were attained for FIB-SEM and nano-CT. However, it is important to note that the field of view for FIB-SEM is typically limited in the slicing direction, since the electron beam focal point shifts with each successive slice and beam stability drops over time. The focal point issue could be resolved by refocusing the electron beam and shifting the field of view progressively upward over the course of the image acquisition sequence (assuming imaging with the SEM source at an off-normal angle). In this work, only about 4 μm of material was captured in the slicing direction, without any refocusing or view shifting. The sample preparation and dataset acquisition took approximately 5–8 h for each of the four FIB-SEM datasets, while the single nano-CT dataset took roughly 35 h to be acquired. In the case of FIB-SEM, the sample preparation and data collection time is determined mostly by the specified FIB current and millability of the tested material, whereas data collection time for nano-CT depends on the inherent contrast of the sample, flux of the source, and efficiency of the X-ray optics [11].

2.2. Image processing and reconstruction

Both FIB-SEM and nano-CT produced a stack of 2-D images composed of pixels of varying grayscale value. Since neither FIB-SEM nor nano-CT is capable of distinguishing the carbon particles from PTFE in the MPL, the carbon particle and PTFE phases were treated as a single solid phase in this study. Prior to segmentation of the FIB-SEM data, several pre-processing procedures were applied to the entire stack of images. For instance, during image acquisition the slice images may be misaligned due to beam shift and/or sample drift. To correct for this issue, the stack of images was aligned using a discrete Fourier transform registration code applied to static/fiducial markers. Once the images were properly aligned, the projection effects, which result from imaging with the SEM source angled at 52° , were corrected by stretching each image vertically and shifting subsequent images downward. The usable portion of the stack was then cropped, and any global gradients were removed using a bi-parabolic surface fit [19]. Additionally, each slice image was coarsened slightly to obtain an image stack with cubic voxels of 20 nm length. For the nano-CT data, the raw radiographs were reconstructed using proprietary software (Xradia, Inc.) into a 3-D tomogram with cubic voxels of 32 nm length, or a stack of grayscale images similar to the FIB-SEM data.

Once the image pre-processing was completed, the datasets were segmented into the solid and void phases to clearly capture the phase distribution in the 3-D reconstructions. Image segmentation was performed using grayscale level thresholding methods for both the FIB-SEM and nano-CT data. The threshold-based segmentation methods utilized in this study included manual thresholding, as well as automated threshold selection schemes such as the ISODATA algorithm [20–22] and Otsu's method [23]. For additional comparison, the FIB-SEM data was also segmented using a fully automated 3-D method developed by Simmons et al. [24], which allows for consideration of both the grayscale value of voxels as well as the classification of neighboring voxels (i.e., pore

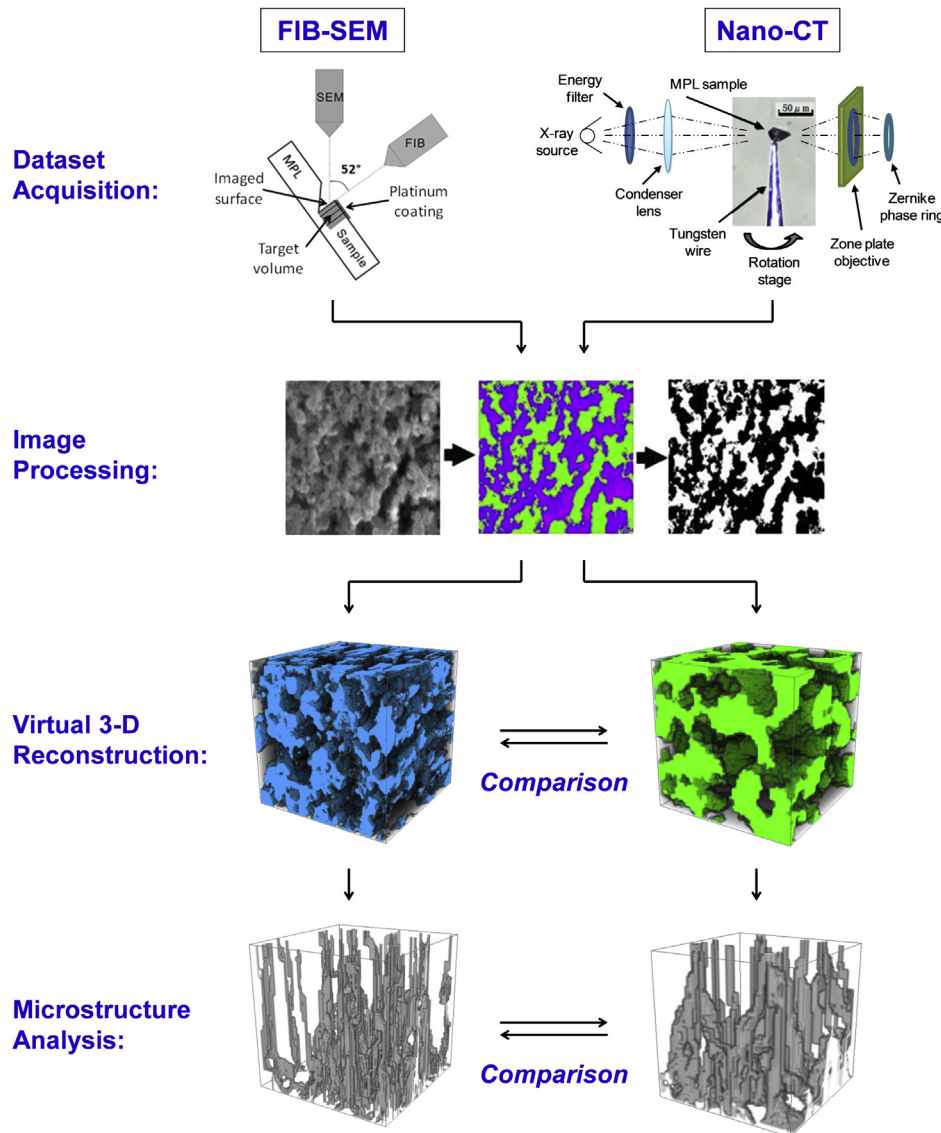


Fig. 1. Flow chart outlining the method of approach of the present study.

vs. solid). This segmentation scheme (referred to as “EM/MPM/SA”) is based on the maximization of posterior marginals (MPM) and incorporates an expectation maximization (EM) algorithm with simulated annealing (SA) [24].

After the datasets were segmented into the desired void and solid phases, each set of images was combined into a stack to form a 3-D microstructure (i.e., reconstruction). As a final step, an island removal procedure was applied to the 3-D reconstructions to identify and remove any isolated agglomerates of solid phase that appeared to be floating in free space. Very few islands (<0.2% of the dataset volume) were found due to the nature of the MPL structure and FIB-SEM/nano-CT data. Detailed descriptions of the image processing, segmentation, and 3-D reconstruction for FIB-SEM datasets may be found in our previous publications [2–4].

2.3. Property (metric) evaluation of microstructure datasets

After the 3-D microstructures of the MPL were reconstructed, several key properties (metrics) were determined for both datasets and compared against each other. The properties used for comparison include the porosity, pore connectivity, tortuosity,

structural diffusivity coefficient, and chord length distributions. The methodologies used to calculate these properties are summarized below. More detailed descriptions of the specific structural analysis protocols can be found in our previous publication [2].

In these analyses, porosity was calculated by taking the ratio of the number of pore voxels to the total number of voxels in the 3-D reconstruction [2–4]. Pore connectivity was determined by first identifying the voxel network within the void space which provides a connection between opposing external faces of the reconstructed volume. These opposing faces may be considered as entry and exit surfaces for transport through the volume. Therefore, any void voxels which do not belong to this “connected” network are considered isolated and unavailable for transport. The pore connectivity was then found by taking the ratio of the number of “connected” void voxels to the total number of void voxels [2–4].

The tortuosity analysis was conducted by computing the shortest path through the pore space from a voxel on the entry surface to the exit surface [2–4]. The tortuosity value of that path was then calculated by taking the ratio of the computed path length to the shortest distance between the entry and exit surfaces (i.e., the thickness of the volume). By evaluating pathways from every

pore voxel on the entry surface, a distribution of tortuosity was resolved for the 3-D microstructure datasets.

Another important parameter used to characterize the measured MPL microstructures was the structural diffusivity coefficient, K . Every material structure possesses a unique resistance to diffusion, which can be reflected through a K value to estimate the effective diffusivity, D_{eff} , of a species of interest:

$$D_{\text{eff}} = K \cdot D_{ij} \quad (1)$$

where D_{ij} is the bulk diffusivity (D_{bulk}) of species i in species j . The value of K was determined using a 3-D diffusion model based on a finite volume approximation of the steady state Fickian diffusion model [2–4]. Each void voxel of the given MPL reconstruction represents a finite volume available for diffusion, with a net flux maintained at zero. Uniform concentrations were held at the entry and exit surfaces, and periodic boundary conditions were applied to the opposing lateral surfaces to prevent any in-plane net flux. The structural diffusivity coefficient was then obtained from the resulting estimate of the through-plane net flux. It should be noted that transport in the MPL of PEFCs is governed partially by Knudsen diffusion [25]; therefore, actual structural diffusivity coefficients might be slightly smaller than those determined by the present model. Nonetheless, the K value determined herein serves as a useful metric for comparing the general diffusive behavior of the measured microstructure datasets.

In order to quantify the size distribution of the pore (void) phase, chord length distributions were calculated for each measured 3-D microstructure. Here, a chord is defined as a line of specific orientation which connects two pore boundaries within the pore structure while lying completely within the pore phase [2,4]. A chord length distribution is calculated for a given orientation by determining the length of every chord in the 3-D voxelated structure within the pore phase [2,4]. Since the chords do not impose an idealized circular/spherical geometry on the phase of interest, chord length distributions can more accurately capture the rough/jagged morphology of porous materials as compared to the conventional approaches. While distributions may be obtained at multiple orientations to increase resolution, only the three primary orthogonal orientations were considered in this study for simplicity.

3. Results and discussion

3.1. Porosity

Porosity is perhaps the most important metric for dataset comparison, since it inevitably affects all structural and transport-related properties for a given class of material. Furthermore, porosity serves as a useful target or as a validation metric during the segmentation of tomographic datasets. In this study, prior to segmentation of the FIB-SEM and nano-CT datasets, the porosity of the MPL sample was determined experimentally using the mass measuring (MM) method and mercury intrusion porosimetry (MIP). The MM and MIP methods yielded porosity values of 0.54 and 0.62 for the tested MPL sample, respectively. Since it is difficult to exclude surface roughness and deformation effects, which cause errors in porosity estimations by MIP, the porosity value of 0.54 obtained by the MM method was used as the target value in this study for comparison during segmentation.

The four FIB-SEM datasets were first segmented using the ISO-DATA method, resulting in porosity values in the range of 0.37–0.38. This tight porosity range, as well as a preliminary metrics analysis using the methods described in Section 2.3, indicate that the four datasets are statistically comparable; therefore, only one

set of raw FIB-SEM data is presented from here on out for simplicity. When the segmented images are analyzed, the resulting ISODATA segmentation looks very reasonable visually (Fig. 2); however, the predicted porosity value of ~ 0.38 is significantly lower than the porosity obtained by the MM technique (~ 0.54). Further segmentation of the FIB-SEM data using Otsu's method and the EM/MPM/SA algorithm yielded similar porosities of 0.39 and 0.40, respectively. When each of these segmentation methods was applied to the nano-CT dataset, the porosity was found to be in the range of 0.54–0.56 which is in good agreement with the porosity value of 0.54 measured by the MM method.

The discrepancy between the auto-segmentation porosity results of the FIB-SEM and nano-CT datasets suggests that the two datasets are quite different from each other, and therefore should not necessarily be segmented in the same manner. While the exact nature of this difference in porosity is unknown, the segmentation results (Fig. 2) suggest that careful consideration should be taken when evaluating the accuracy of raw microstructure datasets obtained by these nanotomography techniques. In particular, this issue appears to be more critical for the FIB-SEM datasets, which have predicted porosities from auto-segmentation in the range of 0.38–0.40 as compared to the experimentally measured value of 0.54. Although the nano-CT auto-segmentation results show good agreement with the MM result, it should be noted that only one dataset was obtained using nano-CT due to the time constraint of the technique, which may pose as some degree of uncertainty. Regardless, the seemingly large porosity discrepancy ($\sim 30\%$) of the FIB-SEM data could stem from several reasons, such as *i*) re-deposition of material on the exposed cross section during FIB serial sectioning; *ii*) erroneous segmentation due to SEM edge effects and uncertainty in distinguishing pore vs. solid, since the internal topography of the pore network is visible; *iii*) erroneous data resulting from solid material which became unsupported and fell off prematurely during serial sectioning; and *iv*) erroneous data due to a large SEM interaction volume. It should also be noted that the FIB-SEM datasets are representative of only $\sim 15 \mu\text{m}$ of the outer thickness of the sample. Therefore, the measured FIB-SEM data could exclude possible regions of higher porosity located in the center of the sample, which would certainly impact the porosity estimated from the FIB-SEM data.

3.2. Comparison of acquired and segmented images

In an effort to effectively compare these two nanotomography techniques, three case studies were performed. For the first two cases, the nano-CT and FIB-SEM datasets were manually thresholded to target the MM porosity (ϵ) of 0.54. These segmented nano-CT and FIB-SEM datasets with $\epsilon = 0.54$ are referred to as Case 1 and Case 2, respectively. As a third case study (Case 3), the FIB-SEM dataset segmented via the ISODATA method ($\epsilon = 0.38$) was also analyzed for further comparison, since this automatically thresholded dataset is believed to better reflect the FIB-SEM data itself. Representative 2-D cross sections from these three cases are shown in Fig. 2.

Fig. 2 shows representative raw grayscale images from the nano-CT and FIB-SEM datasets prior to segmentation with equivalent magnification ratios. The raw nano-CT and FIB-SEM images (Fig. 2, top) look similar in terms of the pore and agglomerate sizes. Regarding their grayscale level histograms, the FIB-SEM curve appears smoother and somewhat tighter with an emerging shoulder, which is useful for segmentation. Conversely, the nano-CT histogram curve appears noisier and much broader with no obvious shoulder, which may complicate segmentation. As shown in Fig. 2, the FIB-SEM segmentation in Case 3 ($\epsilon = 0.38$) seems to capture the pore and void phases of the raw FIB-SEM image fairly well as

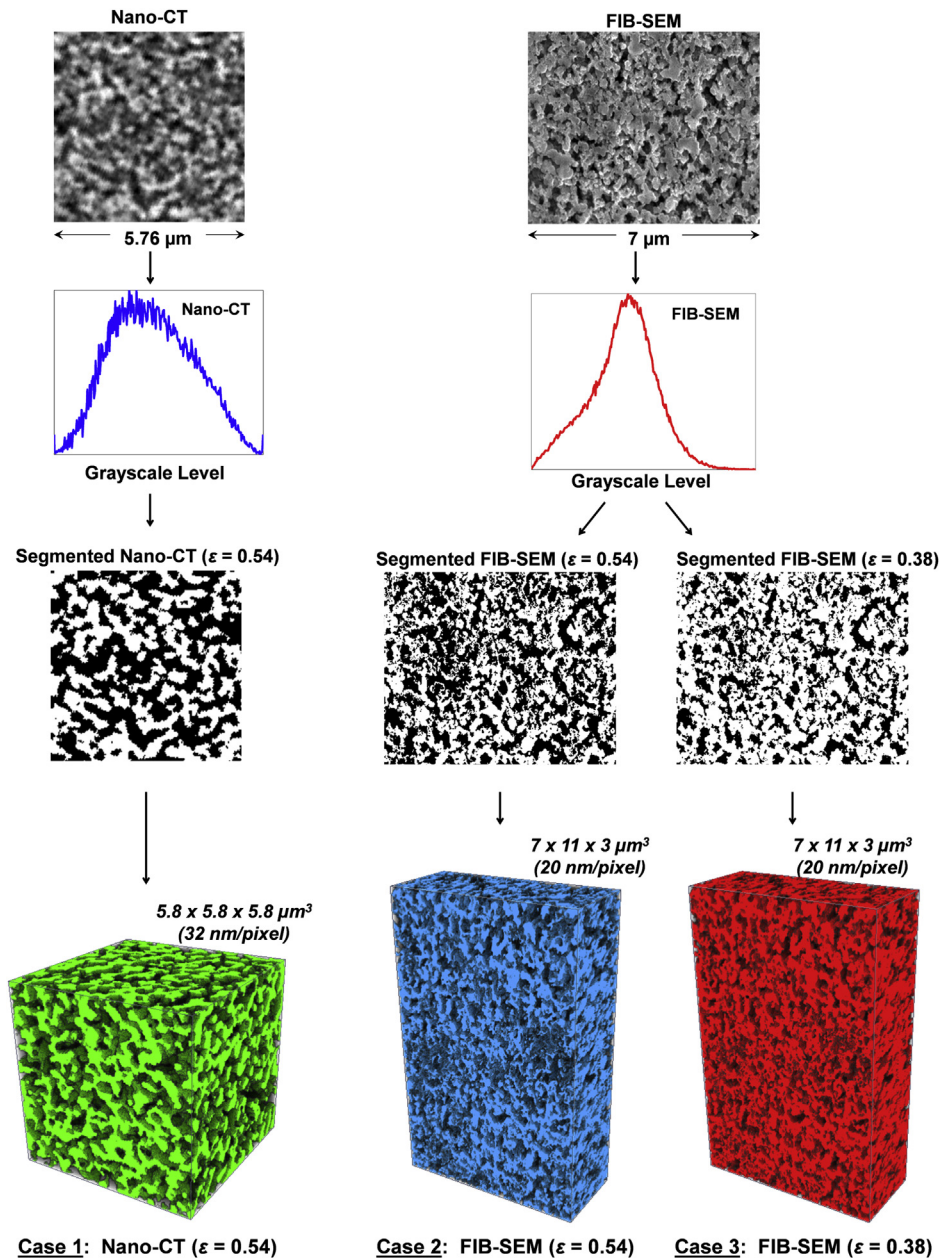


Fig. 2. Comparison of FIB-SEM and nano-CT images, depicted with equivalent magnification ratios. Included are raw FIB-SEM and nano-CT images (top) with their grayscale level histograms, which were segmented to produce dataset Cases 1, 2 and 3. Each image represents a cross section from the corresponding full 3-D dataset (bottom).

compared to Case 2 ($\epsilon = 0.54$), which noticeably misidentifies some regions of solid as void. For Case 1, it is relatively more difficult to visually evaluate the accuracy of the nano-CT segmentation, since the gradients in the raw nano-CT image are fairly smooth with no clear solid/void interface.

Another interesting observation that can be gathered from Fig. 2 is that the segmented nano-CT and FIB-SEM images look noticeably different in terms of phase clustering and feature sizes. This is largely due to the distinct nature of these two datasets. The SEM image captures a single MPL cross section that was physically milled to expose the slice (plane) of interest. Conversely, the nano-CT image represents a cross section of finite thickness, generated from a large number of X-ray radiographs of the entire sample. The higher occurrence of smaller feature sizes in the thresholded FIB-SEM images (Cases 2 and 3) is partially due to the higher resolution (20 vs. 32 nm/pixel), but also appears to result from erroneous

segmentation of darker solid regions within the bright edges of the agglomerates. The bright edges are believed to result from the edge effect of SEM, and their impact is more evident in Case 2. This makes the Case 3 segmentation seem more accurate than Case 2, even though Case 3 drastically undershoots the porosity value of 0.54 obtained using the MM method. It is also difficult to distinguish the void phase from the solid phase in the raw FIB-SEM images, since the internal topography of the pore network beyond the plane of interest is visible due to the depth of field captured by SEM.

Fig. 2 also shows the 3-D reconstructions of the MPL based on the segmented FIB-SEM and nano-CT data for all three cases. Again, there appears to be a higher prevalence of smaller voids and agglomerates in the FIB-SEM datasets (Cases 2 and 3) when compared to the nano-CT dataset (Case 1), but the difference seems less apparent in 3-D. Likewise, the dissimilarity between the two FIB-SEM datasets (Cases 2 and 3) is less obvious when the data is

Table 2
Summary of key structure-related properties for the datasets of Cases 1, 2, and 3, along with relevant experimental values. Tortuosity and structural diffusivity coefficient values are predicted using sets of random volumes selected from the full dataset of each case.

	Case 1: Nano-CT ($\epsilon = 0.54$)	Case 2: FIB-SEM ($\epsilon = 0.54$)	Case 3: FIB-SEM ($\epsilon = 0.38$)	Experimental Units	
Porosity	0.542	0.539	0.377	0.54 (MM ^a) 0.62 (MIP ^b)	Fraction
Pore connectivity	99.9	99.5	99.0	N/A	%
Tortuosity	1.23 \pm 0.022	1.21 \pm 0.024	1.34 \pm 0.028	N/A	Ratio
Structural diffusivity coefficient	0.29 \pm 0.023	0.26 \pm 0.030	0.12 \pm 0.012	N/A	Fraction
Mean pore size	540	365	277	509 (MIP ^b)	nm

^a Determined using the mass measuring (MM) method.
^b Determined using mercury intrusion porosimetry (MIP).

viewed in 3-D. The 3-D reconstructions also indicate the presence of substantial anisotropy in the FIB-SEM data (Cases 2 and 3) with little or no anisotropy visible in Case 1.

3.3. Comparison of metric analysis results

To enable metric (property) analysis of the full 3-D datasets in a reasonable time frame, the microstructure analysis procedures described in Section 2.3 were applied to sets of small, randomly selected volumes (e.g., 25, 50, 75, 100 volumes) from the FIB-SEM and nano-CT datasets. As in our previous studies [2,4], good stabilization was observed for each dataset as the number of volumes increased, which indicates that the datasets were sufficiently sampled. Ultimately, a set of 100 random volumes (each $100 \times 100 \times 100$ pixels³ in size) was selected from identical locations in both the Case 2 and Case 3 datasets to ensure a direct comparison. Similarly, a set of 150 random volumes (each $50 \times 50 \times 50$ pixels³ in size) was selected from the nano-CT dataset

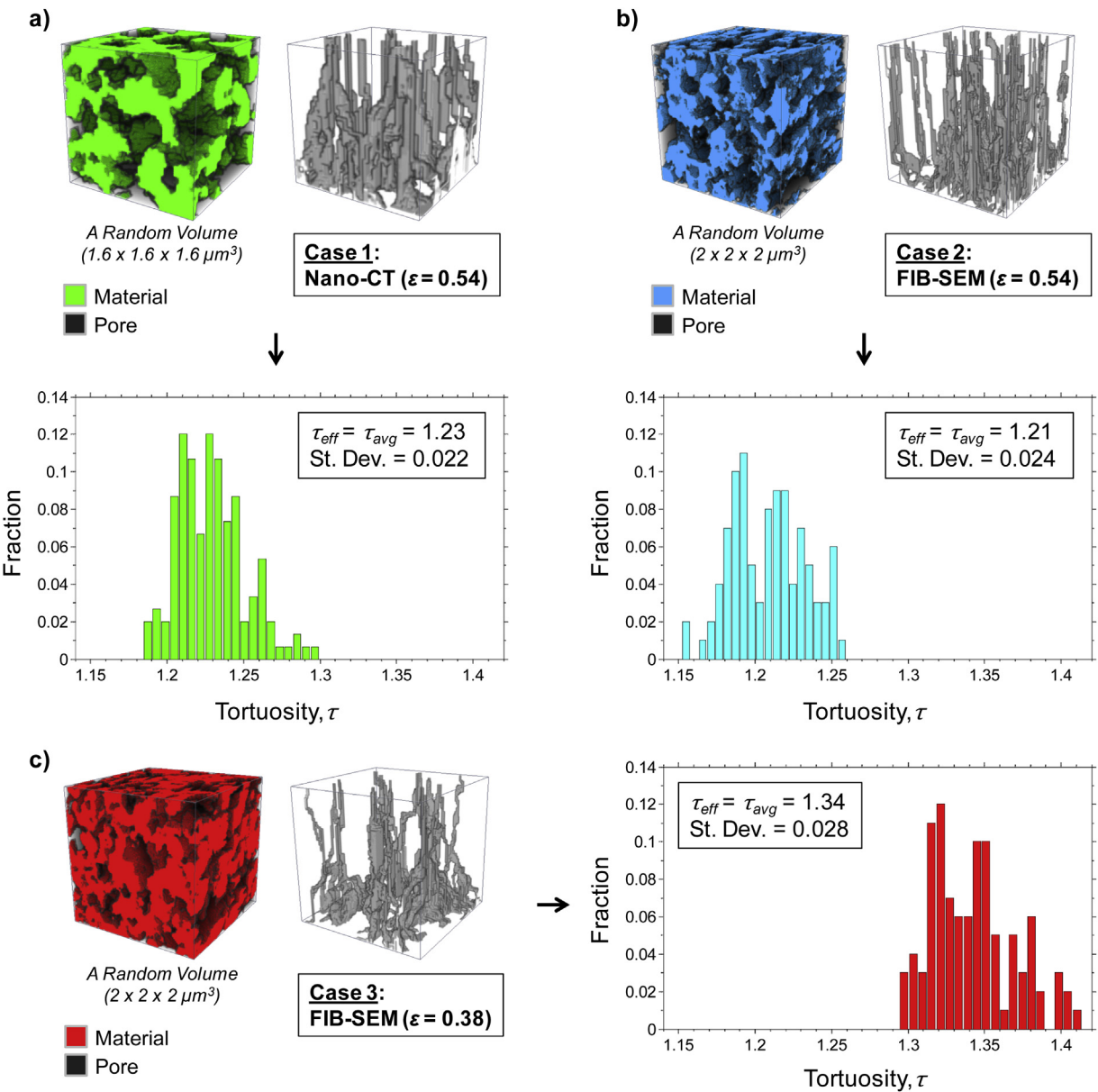


Fig. 3. Tortuosity distributions for a) Case 1, b) Case 2, and c) Case 3. Each distribution is based on many random volumes selected from the full dataset of the corresponding Case. A random volume is shown for each Case for demonstration purposes.

(Case 1). While the size of a random volume for the nano-CT dataset is much smaller than a FIB-SEM volume in terms of pixels, the spatial volumes are more comparable ($1.6 \times 1.6 \times 1.6 \mu\text{m}^3$ for nano-CT and $2 \times 2 \times 2 \mu\text{m}^3$ for FIB-SEM) due to the difference in resolution of these two techniques. Although these sets of small randomly selected volumes were used primarily to speed up the metric analyses (e.g., tortuosity and diffusivity in particular), evaluation of these volume sets also yielded distributions of the properties, which provide insight into the local variation of properties within the tested microstructure. The metric analysis results obtained for Cases 1–3 are summarized in Table 2, along with experimentally determined values.

3.3.1. Pore connectivity and tortuosity analyses

The pore connectivity analysis was performed on the full dataset (i.e., not on random volumes) for all three cases in the through-

plane direction. Each dataset yielded very high connectivity results ($>99\%$ connected), indicating the presence of very few isolated pores in the measured microstructures (Table 2). This suggests that the majority of the pore network in the tested MPL is well-connected and available for mass transport. Among the three cases, the pore connectivity of the nano-CT dataset (Case 1) is observed to be the highest. The pore connectivity of Case 3 is found to be slightly lower than that for Case 2, likely due to the elimination of some small pore throats when attaining the lower porosity; however, at this level of porosity variation, the connectivity of the pore network seems to be affected minimally (only 0.5%).

Fig. 3 shows the through-plane tortuosity distributions computed for each Case. The tortuosity distributions obtained for Case 1 (Fig. 3a) and Case 2 (Fig. 3b) exhibit comparable patterns, with very similar mean tortuosities and standard deviations. This

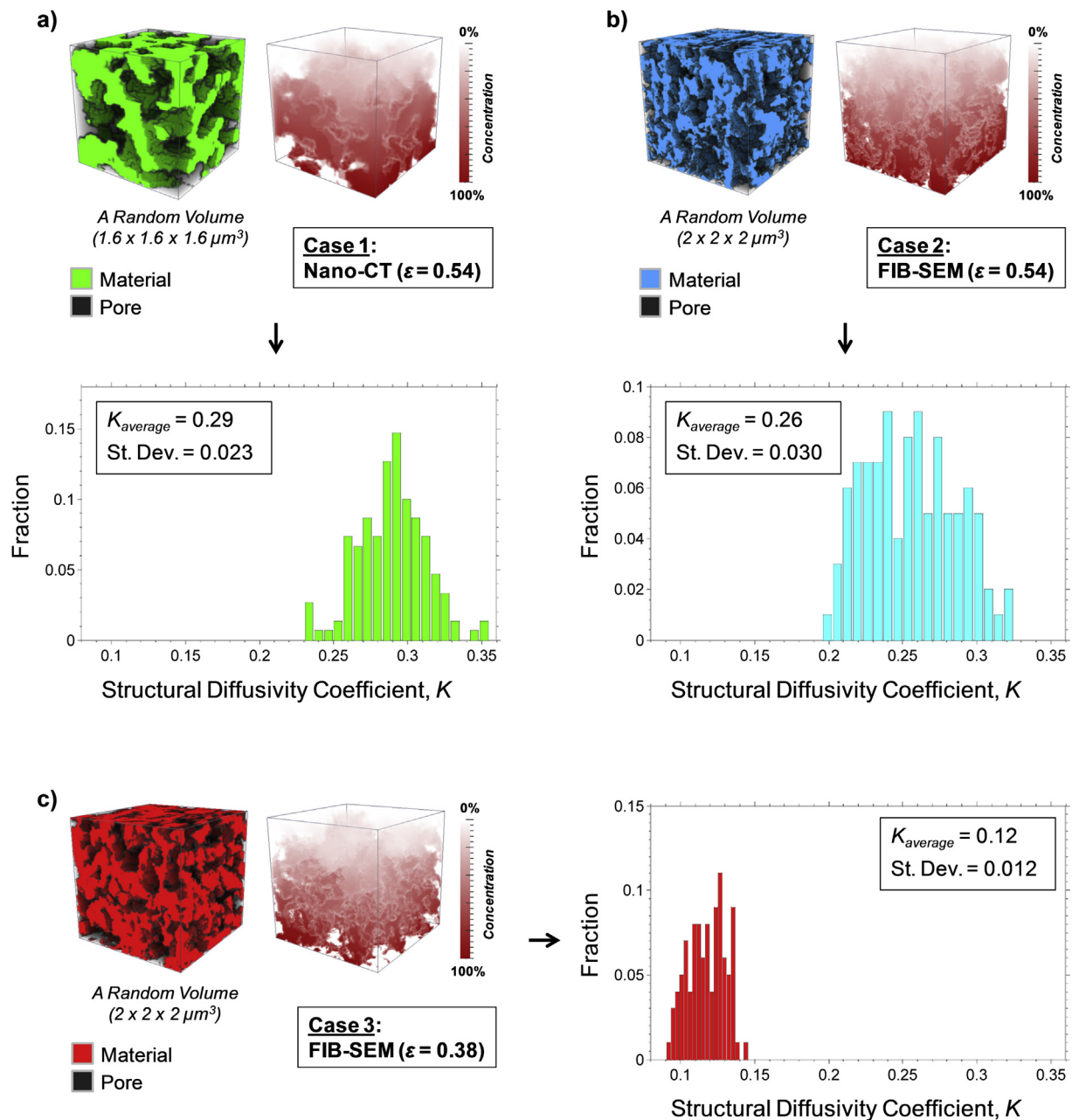


Fig. 4. Structural diffusivity coefficient distributions for a) Case 1, b) Case 2, and c) Case 3. Each distribution is based on many random volumes selected from the full dataset of the corresponding Case. A random volume is shown for each Case for demonstration purposes.

close agreement is partially due to the equivalence of porosity, but also suggests that the FIB-SEM and nano-CT datasets capture similar effects of the MPL microstructure on the connected transport paths through their respective pore networks. The tortuosity distribution of Case 3 (Fig. 3c) is found to be shifted to slightly higher values, with a mean tortuosity value approximately 10% higher than that of Cases 1 and 2. The calculated shortest paths shown in Fig. 3c also appear to be visually lengthier due to the more tortuous nature of this less porous microstructure dataset.

3.3.2. Diffusivity analysis

The diffusivity analysis was conducted on each set of small randomly select volumes in the through-plane direction, and the resulting distributions of structural diffusivity coefficient (K) are shown in Fig. 4. Similar to the tortuosity results, a good agreement is found between the mean values of K for Case 1 (Fig. 4a) and Case 2 (Fig. 4b); however, it is observed that the K distribution of Case 2 is notably broader. Again, the porosity equivalence might be partially responsible for the similar averages of K ; yet the results suggest that the FIB-SEM and nano-CT datasets capture similar microstructures with comparable diffusive resistance. Due to the much lower porosity and more tortuous nature of the Case 3 dataset, its K distribution (Fig. 4c) is observed to be shifted to much lower values, with an average K which is over 50% less than the predicted averages for Cases 1 and 2.

For additional comparison and validation purposes, an effective K value was also determined for each Case by both a computational fluid dynamics (CFD) analysis and a random walk simulation [26]. The value of K is directly resolved from the CFD analysis, which uses the finite volume method. In the case of the random walk simulation (Fig. 5), the average tortuosity (τ_{avg}) of the porous media is obtained as follows. In the 3-D binarized structure, each random walk begins at an arbitrary vacant point (i.e., void voxel) on the start surface, and movement is confined to within the pore (void) phase. Each walker moves one lattice step at a time in an arbitrary direction depending on random numbers. If the walker arrives at the opposite surface, the number of lattice steps is recorded. Thus, in the random walk method, the total number of steps should vary every time the simulation is performed, indicating that many simulations need to be performed to capture the effect of a particular microstructure on mass transport. In this study, the simulation was repeated for 5000 cycles. The average tortuosity was calculated by taking the ratio of the average number of steps for a walker in the porous media versus a walker in an

equivalent volume of free space. This average tortuosity was then input into the following effective medium approximation [27] to solve for K :

$$\frac{\varepsilon}{\tau_{avg}} = \frac{D_{eff}}{D_{bulk}} = K \quad (2)$$

Both the CFD analysis and random walk simulation showed good agreement with the finite volume analysis presented in this study. For example, the CFD, random walk, and finite volume analyses yielded effective K values of 0.286, 0.281, and 0.289, respectively for the nano-CT dataset.

3.3.3. Chord length analysis

Chord length distributions (CLDs) were calculated for the full MPL microstructure datasets of each Case and are shown in Fig. 6. Each plot includes CLDs for the three primary orthogonal orientations, along with the computed average CLD based on the three orientations. As shown in Fig. 6, the chord length distributions of Cases 1, 2, and 3 are noticeably different from each other. Moving from Case 1 to Case 3, the mean chord length (mean pore size) value decreases and the distributions get progressively tighter and skewed more to the left. Among the cases studied, the CLD of the nano-CT dataset (Case 1, Fig. 6a) is found to be the broadest and skewed toward the larger chord lengths. Additionally, the CLDs and mean pore sizes of Cases 1 and 2 are observed to be significantly different, despite the equivalence of porosity and similar effective tortuosity values and structural diffusivity coefficients. This observation can be partially attributed to the higher resolution of the FIB-SEM data, as well as the presence of large regions of neighboring voxels with grayscale levels bordering the threshold value that was used for segmentation (i.e., these regions result in many small black and white clusters in the segmented FIB-SEM data). Furthermore, Cases 2 and 3 appear to be fairly anisotropic, while the nano-CT dataset (Case 1) is nearly isotropic when considering the distributions for the x , y , and z orientations. The anisotropy of Cases 2 and 3 is likely due to the serial sectioning process used to acquire the FIB-SEM data, in which some solid material could fall prematurely from beyond the slice (plane) of interest, resulting in pores which are longer in the slicing direction (z). The anisotropy and smaller pore sizes observed in the FIB-SEM data may also be caused by erroneous segmentation due to the edge effects and depth of field present in the SEM images, as well as redeposition of solid material during serial sectioning.

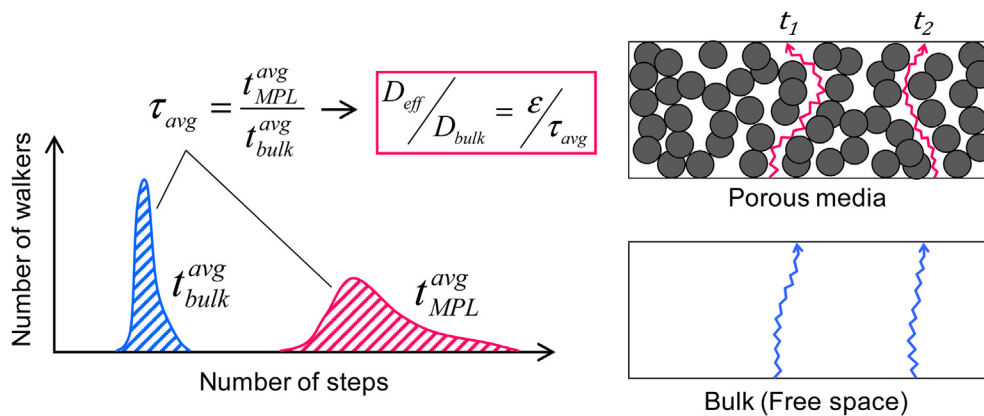


Fig. 5. The random walk simulation tracks a large number of “walker” particles as they travel through i) the measured microstructure of the porous media and ii) an equivalent volume of free space. The number of steps is proportional to the length of the transport paths. The path length data from the two simulations are used to compute an average tortuosity (τ_{avg}) for the material, which is then used to determine the K value with Eq. (2).

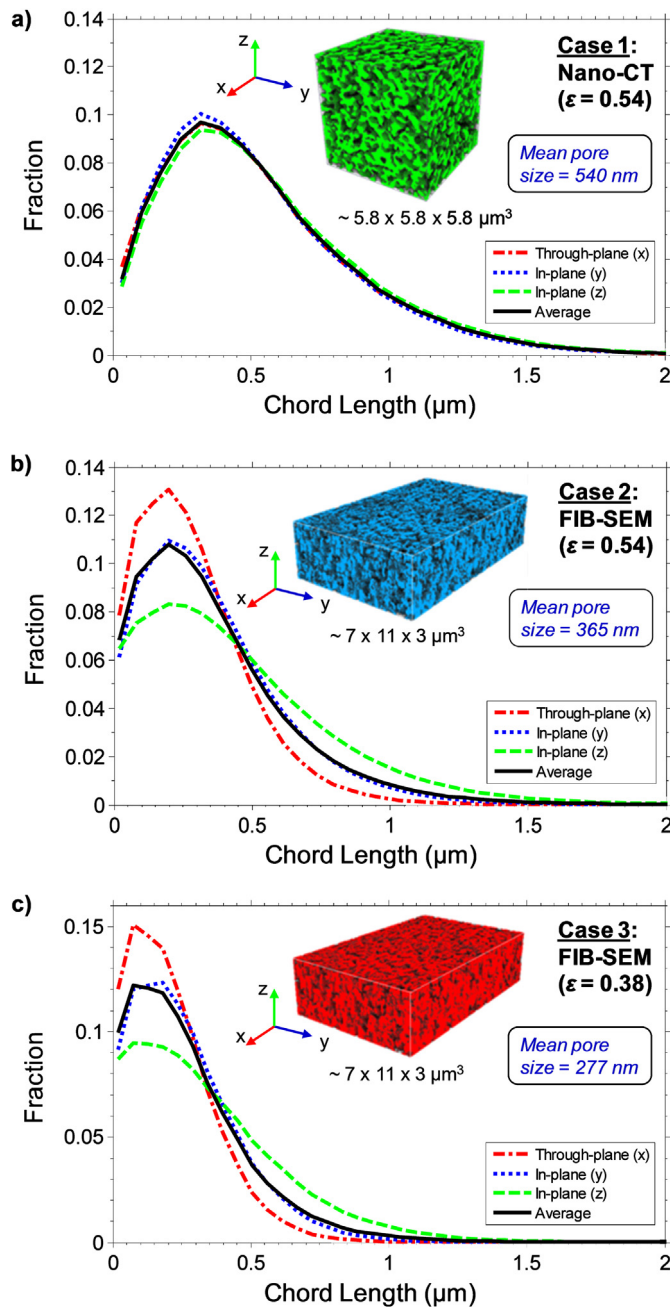


Fig. 6. Chord length distributions for the pore (void) phase of a) Case 1, b) Case 2, and c) Case 3. Distributions in the three primary orthogonal directions and the average of the three distributions are included for each dataset.

In addition to obtaining an estimate for the porosity, MIP was also used to achieve a pore size distribution for the tested MPL sample, as shown in Fig. 7. The MIP results show a peak pore size around 120 nm, and suggest a mean pore diameter of 509 nm when the data above 10 μm is excluded. The MIP data above 10 μm is attributed to the surface roughness effects of the material. In addition, the MIP method assumes cylindrical pores, which likely misrepresents the rough/jagged internal morphology of the tested MPL microstructure. While it is difficult to completely remove the surface roughness, deformation, and other geometry effects in MIP data, the mean pore size estimation of 509 nm is comparable to the CLD analyses, which showed a mean chord length (mean pore size) of 540 nm, 365 nm, and 277 nm for Cases 1, 2, and 3, respectively.

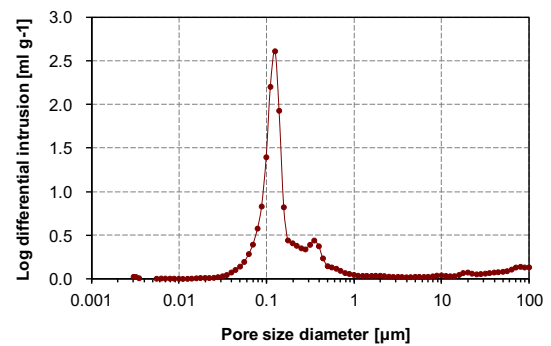


Fig. 7. Pore size distribution of the tested MPL sample measured via mercury intrusion porosimetry (MIP).

4. Conclusion

In this work, 3-D microstructure data was captured for an MPL sample using both nano-CT and FIB-SEM to compare these two nanotomography techniques. While the raw grayscale images of both datasets appeared to be similar visually in terms of pore and agglomerate sizes, automated segmentation of the two datasets yielded significantly different porosity values. The segmented FIB-SEM data yielded a much lower predicted porosity (0.38–0.40) and noticeably different microstructure, as compared to the nano-CT data (0.54–0.56), which is in good agreement with the experimentally measured value of 0.54. When the FIB-SEM and nano-CT datasets were segmented to target the experimentally measured porosity of 0.54, subsequent metric analyses yielded encouragingly similar results for the pore connectivity, tortuosity, and structural diffusivity coefficient (K). However, the chord length (i.e., pore size) distributions of the FIB-SEM data showed significantly smaller values and more anisotropy as compared to the nano-CT data. Although the exact cause of this discrepancy between the FIB-SEM and nano-CT data is unknown, several items for consideration are highlighted below to promote best practices.

First, while auto-segmentation of the nano-CT data yielded a porosity value in good agreement with the experimentally measured value, only one dataset was obtained using nano-CT due to the relatively high cost and time associated with the device. Furthermore, the FIB-SEM datasets are representative of only the outer 15% of the sample with respect to the thickness. Therefore, it is possible that the FIB-SEM and nano-CT data are not statistically comparable. If we assume that this is not the case, the results overall seem to indicate that the nano-CT data better reflects the microstructure and structure-related transport properties of the tested MPL sample. However, analyses of more samples with different features need to be performed to further support this observation.

The seemingly less representative quality of the FIB-SEM data could have several causes, such as i) re-deposition of material on the exposed cross section during FIB serial sectioning; ii) erroneous segmentation due to SEM edge effects and uncertainty in distinguishing pore vs. solid, since the internal topography of the pore network is visible; iii) erroneous data resulting from solid material which became unsupported and fell off prematurely during serial sectioning; and iv) erroneous data due to a large SEM interaction volume. Some of these issues could be minimized by impregnating the sample with a contrast material, which may alleviate the effects listed in items (ii) and (iii) above. Many of these items are also likely culprits for the anisotropy found in the FIB-SEM data. Additionally, the smaller pore sizes seen in the FIB-SEM data may be attributed to the higher resolution of the dataset, as well as the presence of large

regions of neighboring voxels with grayscale levels bordering the threshold value used for segmentation. Such regions of “noise” in the raw SEM images result in many small black and white clusters in the segmented FIB-SEM data. This noise could be minimized through post-processing of the raw images (e.g., using a median filter) or possibly reduced during SEM image acquisition.

Although nano-CT appears to outperform FIB-SEM regarding the accuracy of the data acquired in this study, the acquisition and processing of FIB-SEM data has much room for improvement as highlighted in this work. When properly employed, FIB-SEM is potentially a more powerful technique for acquiring 3-D microstructure data, as it is generally faster and has imaging/resolution capabilities which are currently unattainable by nano-CT.

Acknowledgments

EAW would like to thank the Department of Defense for support through the National Defense Science & Engineering Graduate Fellowship (NDSEG) Program. In addition, support from the National Science Foundation (grant no. DMR-0722845) is acknowledged for instrumentation.

References

- [1] H. Ostadi, P. Rama, Y. Liu, R. Chen, X.X. Zhang, K. Jiang, *Journal of Membrane Science* 351 (2010) 69–74.
- [2] A. Cecen, E.A. Wargo, A.C. Hanna, D.M. Turner, S.R. Kalidindi, E.C. Kumbur, *Journal of the Electrochemical Society* 159 (3) (2012) B299–B307.
- [3] E.A. Wargo, A.C. Hanna, A. Cecen, S.R. Kalidindi, E.C. Kumbur, *Journal of Power Sources* 197 (2012) 168–179.
- [4] E.A. Wargo, V.P. Schulz, A. Cecen, S.R. Kalidindi, E.C. Kumbur, *Electrochimica Acta* 87 (2013) 201–212.
- [5] C. Ziegler, S. Thiele, R. Zengerle, *Journal of Power Sources* 196 (2011) 2094–2097.
- [6] S. Zils, M. Timpel, T. Arlt, A. Wolz, I. Manke, C. Roth, *Fuel Cells* 10 (2010) 966–972.
- [7] W.K. Epting, J. Gelb, S. Litster, *Advanced Functional Materials* 22 (2012) 555–560.
- [8] F. Lasagni, A. Lasagni, M. Engstler, H.P. Degischer, F. Mücklich, *Advanced Engineering Materials* 10 (2008) 62–66.
- [9] H. Ostadi, M. Malboubi, P.D. Prewett, K. Jiang, *Microelectronic Engineering* 86 (2009) 868–870.
- [10] N.S.K. Gunda, H.W. Choi, A. Berson, B. Kenney, K. Karan, J.G. Pharoah, S.K. Mitra, *Journal of Power Sources* 196 (2011) 3592–3603.
- [11] P.R. Shearing, J. Gelb, N. Brandon, *ECS Transactions* 19 (17) (2009) 51–57.
- [12] B. Rüger, J. Joos, A. Weber, T. Carraro, E. Ivers-Tiffée, *ECS Transactions* 25 (2) (2009) 1211–1220.
- [13] H. Iwai, N. Shikazono, T. Matsui, H. Teshima, M. Kishimoto, R. Kishida, D. Hayashi, K. Matsuzaki, D. Kanno, M. Saito, H. Muroyama, K. Eguchi, N. Kasagi, H. Yoshida, *Journal of Power Sources* 195 (2010) 955–961.
- [14] P.R. Shearing, J. Gelb, J. Yi, W.-K. Lee, M. Drakopoulos, N.P. Brandon, *Electrochemistry Communications* 12 (2010) 1021–1024.
- [15] C.A. Volkert, A.M. Minor, *MRS Bulletin* 32 (2007) 389–399.
- [16] M. Manahan, M.C. Hatzell, E.C. Kumbur, M.M. Mench, *Journal of Power Sources* 196 (2011) 5573–5582.
- [17] J. Roth, J. Eller, F.N. Büchi, *Journal of the Electrochemical Society* 159 (8) (2012) F449–F455.
- [18] J. Eller, T. Rosen, F. Marone, M. Stampanoni, A. Wokaun, F.N. Büchi, *Journal of the Electrochemical Society* 158 (8) (2011) B963–B970.
- [19] V. Pastushenko, SURFIT. <http://www.mathworks.com/matlabcentral/fileexchange/6244>, MATLAB Central File Exchange, 18 Nov 2004.
- [20] G.H. Ball, D.J. Hall, *ISODATA, a Novel Method of Data Analysis and Pattern Classification*, Stanford Research Institute, Menlo Park, CA, 1965. Technical Report AD 699616.
- [21] T.W. Ridler, S. Calvard, *IEEE Transactions: Systems, Man, and Cybernetics SMC-8* (1978) 630–632.
- [22] D. Ramachandram, *Automatic Thresholding*. <http://www.mathworks.com/matlabcentral/fileexchange/3195>, MATLAB Central File Exchange, 31 Mar 2003.
- [23] N. Otsu, *IEEE Transactions: Systems, Man, and Cybernetics SMC-9* (1979) 62–66.
- [24] J.P. Simmons, P. Chuang, M. Comer, J.E. Spowart, M.D. Uchic, M. De Graef, *Modelling and Simulation in Materials Science and Engineering* 17 (2009) 025002.
- [25] L.M. Pant, S.K. Mitra, Marc Secanell, *Journal of Power Sources* 206 (2012) 153–160.
- [26] G. Inoue, Y. Matsukuma, M. Minemoto, *ECS Transactions* 25 (1) (2009) 1519–1527.
- [27] K. Jiao, X. Li, *Progress in Energy and Combustion Science* 37 (2011) 221–291.